AIAA JOURNAL
Vol. 42, No. 10, October 2004

Azimuthal Sound Mode Propagation in Axisymmetric Flow Ducts

X. D. Li*
Beijing University of Aeronautics and Astronautics, 100083 Beijing, People's Republic of China
C. Schemel†
Berlin University of Technology, D-10623 Berlin, Germany
U. Michel‡
DLR, German Aerospace Research Center, D-10623 Berlin, Germany
and
F. Thiele§
Berlin University of Technology, D-10623 Berlin, Germany

Assuming an axisymmetric mean flow and acoustic boundary conditions, a set of three-dimensional axisymmetric equations suitable for each azimuthal sound mode of fluctuation is derived based on the three-dimensional linearized Euler equations. The independent two-dimensional model for each azimuthal sound mode is deduced by a Fourier series decomposition. A computational aeroacoustics approach is then applied to solve each two-dimensional equation system. The dispersion-relation-preserving finite difference scheme is implemented for spatial discretization, whereas the 2*N* storage low-dissipation and low-dispersion Runge–Kutta scheme is applied for time integration. Appropriate boundary conditions are prescribed at the various boundary regions. The numerical procedure is first validated by cases of a straight circular pipe and an annular duct subjected to a subsonic uniform mean flow, the numerical results of which show very good agreement with the analytical solutions. A further numerical example is presented for an axisymmetric inlet duct with an aeroenginelike geometry including an internal spinner. The aeroacoustic computation is based on an inviscid irrotational mean flow calculated by a second-order computational fluid dynamics solver. The acoustic solutions agree well with the existing finite element and multiple-scales solutions in the literature. Finally, the cuton, cutoff transition phenomena are investigated based on the proposed numerical approach. The transition behavior is found to be highly dependent on the mean flowfield in addition to the known geometric effect. These results demonstrate the feasibility of the proposed model and solution procedure.

Nomenclature

A_{mn}	=	complex amplitude of the sound source
A, B, C, D	=	matrices incorporating the spatial and mean flow derivatives to the acoustic field
a_i	=	stencil coefficients of the dispersion-relation-preserving finite difference scheme ($i = -3, 3$)
a_∞, ϱ_∞	=	typical sound speed and density, respectively
b_{nt}	=	Gaussian half-width of a buffer zone
$\boldsymbol{F}_x, \boldsymbol{F}_r, \boldsymbol{F}_\varphi, \boldsymbol{G}$	=	vectorlike functions of $\boldsymbol{Q}$ for the spatial derivatives
i	=	$\sqrt{-1}$
J_m	=	mth-order Bessel function of the first kind
k	=	axial wave number
$k(q)$	=	flux of the differential equations
L	=	length of a duct
M_x	=	local mean flow Mach number
m	=	azimuthal acoustic mode number
n	=	radial acoustic mode number
$\boldsymbol{n}$	=	normal vector
$\bar{p}$	=	mean flow pressure
p'	=	pressure fluctuation
$\boldsymbol{Q}, \boldsymbol{q}$	=	vector of conservative and primitive dependent acoustic field variables, respectively
q	=	primitive dependent acoustic field variables
q_0	=	basic states of primitive dependent variables
$R_d^{-1}(x)$	=	reduction coefficient of Newtonian friction
$\Re\mathfrak{e}\{\}$	=	real part of the complex variables
R_1, R_2	=	outer and inner wall radius of ducts
R_∞	=	typical duct radius
t	=	time
$\bar{U}, \bar{V}, \bar{W}$	=	components of the mean flow velocity in x, r, φ directions, respectively
u', v', w'	=	components of the velocity fluctuation in x, r, φ directions, respectively
$\boldsymbol{V}$	=	contravariant velocity
x, r, φ	=	components of the cylindrical coordinate system
x_B	=	x coordinates of terminal plane
x'	=	function of x and L
Y_m	=	mth-order Neumann function
λ	=	acoustic wavelength
μ_{mn}	=	radial wave eigenvalue of azimuthal mode m with radial order n
ξ	=	cutoff ratio
$\bar{\rho}$	=	mean flow density
ϱ'	=	density fluctuation
ω	=	angular frequency

Presented as Paper 2002-2521 at the AIAA/CEAS 8th Aeroacoustics Conference, Breckenridge, CO, 17–19 June 2002; received 20 July 2002; accepted for publication 13 January 2004.

*Professor, School of Jet Propulsion, Xueyuan Street 37. Senior Member AIAA.
†Research Engineer, Hermann-Foettinger-Institute of Fluid Mechanics, Strasse des 17. Juni 135.
‡Senior Scientist, Section Turbulence Research Berlin, Institute of Propulsion Technology, Mueller-Breslau-Strasse 8.
§Professor, Hermann-Foettinger-Institute of Fluid Mechanics, Strasse des 17. Juni 135.

Introduction

FAN tones are known to be an important noise component of modern high-bypass-ratio aeroengines. To accurately evaluate the sound propagation in an aeroengine inlet and the far-field radiation thereof, the prediction methods must be capable of handling complex geometries, including the spinner, and variable cross section and of accounting for basic mean flow effects. In

general, fully three-dimensional numerical methods[1–4] are required for the calculation of sound propagation in a duct. The main disadvantage is that three-dimensional methods, especially for high-frequency cases, have high costs, both of time consumption and of the computational resources demanded.

This paper addresses small-amplitude sound propagation in axisymmetric duct flows. The three-dimensional linearized Euler equations in a cylindrical coordinate system (x, r, φ) could be used to describe this problem. However, under the assumption of an axisymmetric mean flow and axisymmetric acoustic boundary conditions, the three-dimensional fluctuating quantities can be decomposed into a Fourier series in the azimuthal direction. This transform of the independent variable φ to the azimuthal mode number m yields a system of independent two-dimensional (x, r) differential equations for each azimuthal mode m of the fluctuations. Because tone noise in the inlet of aircraft engines is generally dominated by only a few components at the blade-passing frequency and its harmonics plus harmonics of the shaft frequency (in the case of buzz-saw noise), it is computationally much more efficient to treat these few two-dimensional Fourier components rather than to solve the full three-dimensional system. In fact, the Fourier decomposition technique has found various applications in axisymmetric duct acoustics. For example, it was employed in the finite element method (FEM) of Eversman et al.[5] and the multiple-scales (MS) method of Rienstra.[6]

The approach proposed in this paper is a hybrid numerical procedure. The two-dimensional axisymmetric mean flow is first calculated by a low-order computational fluid dynamics (CFD) method through solution of the Euler equations. Then the acoustic field is computed by a high-order computational aeroacoustic (CAA) approach through solution of each component of the derived three-dimensional axisymmetric system. Usually the models of MS,[6] FEM,[5] boundary element,[7] and finite and infinite element[8,9] prefer the choice of frequency domain because they are technically easier to deal with for single-frequency problems and only the convected Helmholtz equation is considered as the governing equation. However, the time domain method has gained more favor in CAA simulations[1,2] due to the convenience on broadband noise predictions as well as on solving complex equation systems. To develop a more general numerical procedure, a time domain method is chosen to solve the derived governing equations in this paper.

The proposed CFD/CAA numerical procedure is first validated by comparison with the analytical solutions in a circular and an annular duct with a uniform mean flow. Then two typical numerical results are given for an aeroengine inlet duct geometry and benchmarked against the results of FEM and MS methods.[10] To show the capability of the CFD/CAA hybrid method, the acoustic hard-walled duct cuton and cutoff transition phenomenon is studied numerically for the same aeroengine duct inlet geometry. Much attention is paid to the sensitivity of the transition plane to the basic mean flow assumptions with a one-dimensional potential flow and a two-dimensional Euler mean flow, respectively. The contents of this paper are organized in the following manner: The mathematical model is first presented with a derivation of the governing equations and the description of the basic hybrid procedure. Then the detailed numerical algorithm is described with special attention to boundary conditions. The numerical validation and investigation cases are detailed in the Results and Discussion section. Finally a conclusion on the presented results is given.

Mathematical Model

Concerning the propagation of small-amplitude sound waves in a cylindrical or annular duct with subsonic inviscid mean flow without swirl ($\bar{W} = 0$), the linearized three-dimensional Euler equations specialized to cylindrical coordinates are selected as the starting point:

$$\frac{\partial \boldsymbol{Q}}{\partial t} + \frac{\partial \boldsymbol{F}_x}{\partial x} + \frac{\partial \boldsymbol{F}_r}{\partial r} + \frac{1}{r}\frac{\partial \boldsymbol{F}_\varphi}{\partial \varphi} + \frac{\boldsymbol{G}}{r} = 0 \tag{1}$$

where the vectors $\boldsymbol{Q}$, $\boldsymbol{F}_x$, $\boldsymbol{F}_r$, $\boldsymbol{F}_\varphi$, and $\boldsymbol{G}$ are given by the acoustic and mean flowfield state:

$$\boldsymbol{Q} = \begin{pmatrix} \varrho' \\ \hat{u}' \\ \hat{v}' \\ \hat{w}' \end{pmatrix} = \begin{pmatrix} \varrho' \\ \bar{\varrho}u' + \varrho'\bar{U} \\ \bar{\varrho}v' + \varrho'\bar{V} \\ \bar{\varrho}w' \end{pmatrix}, \qquad \boldsymbol{F}_x = \begin{pmatrix} \hat{u}' \\ 2\bar{U}\hat{u}' - \bar{U}^2\varrho' + p' \\ \bar{U}\hat{v}' + \bar{V}\hat{u}' - \bar{U}\bar{V}\varrho' \\ \bar{U}\hat{w}' \end{pmatrix}$$

$$\boldsymbol{F}_r = \begin{pmatrix} \hat{v}' \\ \bar{U}\hat{v}' + \bar{V}\hat{u}' - \bar{U}\bar{V}\varrho' \\ 2\bar{V}\hat{v}' - \bar{V}^2\varrho' + p' \\ \bar{V}\hat{w}' \end{pmatrix}, \qquad \boldsymbol{F}_\varphi = \begin{pmatrix} \hat{w}' \\ \bar{U}\hat{w}' \\ \bar{V}\hat{w}' \\ p' \end{pmatrix}$$

$$\boldsymbol{G} = \begin{pmatrix} \hat{v}' \\ \bar{U}\hat{v}' + \bar{V}\hat{u}' - \bar{U}\bar{V}\varrho' \\ 2\bar{V}\hat{v}' - \bar{V}^2\varrho' \\ 0 \end{pmatrix}$$

Assuming a homentropic mean flow and neglecting heat conduction, the isentropic law can be used to link pressure and density perturbations:

$$p' = \gamma(\bar{p}/\bar{\varrho})\varrho' \tag{2}$$

Equations (1) and (2) are given in nondimensional form. The length scales x, r are nondimensionalized by a typical duct radius R_∞; the velocity components u', v', w', $\bar{U}$, $\bar{V}$, and $\bar{W}$ by the typical speed of sound a_∞; the time t by R_2/a_∞; the densities ϱ' and $\bar{\rho}$ by the typical density ρ_∞; and the pressures p' and $\bar{p}$ by the product of the typical speed of sound squared and density $\rho_\infty a_\infty^2$.

The dependency of the sound field on the azimuthal coordinate φ is described by a Fourier series of m, e.g., for the pressure:

$$p'(t, x, r, \varphi) = p'_m(t, x, r)e^{-im\varphi} \tag{3}$$

Considering an axisymmetric duct geometry with axisymmetric mean flow and expanding Eq. (1) with the approach equation (3), a set of fully decoupled only two-dimensional-dependent (x, r) governing equations for a single mode can be found. They are rewritten in matrix-vector form:

$$\frac{\partial \boldsymbol{q}}{\partial t} = -A \cdot \frac{\partial \boldsymbol{q}}{\partial x} - B \cdot \frac{\partial \boldsymbol{q}}{\partial r} - \frac{1}{r}C \cdot \boldsymbol{q} - D \cdot \boldsymbol{q} \tag{4}$$

with

$$A = \begin{pmatrix} \bar{U} & \bar{\varrho} & 0 & 0 & 0 \\ 0 & \bar{U} & 0 & 0 & \dfrac{1}{\bar{\varrho}} \\ 0 & 0 & \bar{U} & 0 & 0 \\ 0 & 0 & 0 & \bar{U} & 0 \end{pmatrix}, \qquad B = \begin{pmatrix} \bar{V} & 0 & \bar{\varrho} & 0 & 0 \\ 0 & \bar{V} & 0 & 0 & 0 \\ 0 & 0 & \bar{V} & 0 & \dfrac{1}{\bar{\varrho}} \\ 0 & 0 & 0 & \bar{V} & 0 \end{pmatrix}$$

$$C = \begin{pmatrix} \bar{V} & 0 & \bar{\varrho} & -im\bar{\varrho} & 0 \\ 0 & 0 & 0 & 0 & 0 \\ 0 & 0 & 0 & 0 & 0 \\ 0 & 0 & 0 & \bar{V} & -i\dfrac{m}{\bar{\varrho}} \end{pmatrix}$$

$$D = \begin{pmatrix} \dfrac{\partial \bar{U}}{\partial x} + \dfrac{\partial \bar{V}}{\partial r} & \dfrac{\partial \bar{\varrho}}{\partial x} & \dfrac{\partial \bar{\varrho}}{\partial r} & 0 & 0 \\ \dfrac{1}{\bar{\varrho}}\left(\bar{U}\dfrac{\partial \bar{U}}{\partial x} + \bar{V}\dfrac{\partial \bar{U}}{\partial r}\right) & \dfrac{\partial \bar{U}}{\partial x} & \dfrac{\partial \bar{U}}{\partial r} & 0 & 0 \\ \dfrac{1}{\bar{\varrho}}\left(\bar{U}\dfrac{\partial \bar{V}}{\partial x} + \bar{V}\dfrac{\partial \bar{V}}{\partial r}\right) & \dfrac{\partial \bar{V}}{\partial x} & \dfrac{\partial \bar{V}}{\partial r} & 0 & 0 \\ 0 & 0 & 0 & 0 & 0 \end{pmatrix}$$

and $\boldsymbol{q} = (\varrho'_m, u'_m, v'_m, w'_m, p'_m)^T$. The closing equation (2) becomes

$$p'_m = \gamma(\bar{p}/\bar{\varrho})\varrho'_m \tag{5}$$

For handling complex geometries, the governing equations are solved in generalized curvilinear coordinates by a CAA method so that body-fitted computational meshes can be used conveniently. The required background mean flow is separately calculated by a low-order finite volume CFD method using the Euler equations. In particular, the mean flow entropy is assumed to be constant for consistency with the homentropic assumption given earlier [$\bar{p} = \bar{p}(\bar{\varrho})$].

In summary, the resulting CFD/CAA numerical method consists of the following four steps: 1) calculation of the inviscid homentropic mean flowfield by a CFD method, 2) Fourier decomposition of the three-dimensional sound source into azimuthal sound modes, 3) CAA computation of the sound propagation for each mode, and 4) recomposing the computed solutions to a three-dimensional sound field using the inverse Fourier transform if required, such as to construct an integration surface for far-field computation.

It should be pointed out that the proposed model can be extended to be suitable for nonhomentropic mean flow cases by replacing Eq. (2) with a linearized entropy equation. A set of governing equations including swirl ($\bar{W} \neq 0$) can also be derived. The resulting approach will be valid for the bypass duct of an aeroengine as well.

Numerical Algorithm

Discretization Scheme

To solve the three-dimensional axisymmetric governing equations (4) and (5), a CAA approach is developed. It is important to select numerical schemes having high resolution and low dispersion and dissipation in both space and time discretization. The well-known seven-point fourth-order dispersion-relation-preserving (DRP) finite difference scheme by Tam and Webb[11] is employed for space discretization. In the interior field, the fourth-order centralized stencil coefficients are selected as $a_0 = 0$, $a_1 = -a_{-1} = 0.770882380518$, $a_2 = -a_{-2} = 0.166705904415$, and $a_3 = -a_{-3} = 0.0208431427703$. At the boundary region, backward stencil coefficients are implemented. Detailed information can be found in the review paper by Tam.[12] The DRP scheme can resolve sound waves approximately seven points per wavelength (PPW) with little dispersion and dissipation. The solution is advanced in time by the $\frac{5}{6}$ low-dissipation and low-dispersion Runge–Kutta method[13] in the $2N$ storage form.[14] Because the centralized DRP scheme has been applied, the selective artificial damping technique[15] is adopted to eliminate spurious short-wavelength signals excited from boundaries or stretched grids.

Boundary Conditions

Numerical computations can be performed only in a finite domain size. Considering an aeroengine intake geometry as shown in Fig. 1, appropriate boundary conditions (BCs) must be correctly implemented for each boundary including the inflow, sound source, hard wall, and axis of the cylindrical coordinate system. Detailed information for the BCs is given next.

Inflow BC

In this paper, we focus on the upstream propagation of acoustic modes through ducts with subsonic mean flow. It is assumed that there is no reflection from the inflow boundary region. To prevent reflections, a Newtonian cooling/friction-based damping layer buffer zone[16,17] is introduced at the inflow boundary region. The principle is to absorb all of the upstream-propagating disturbances in the buffer zone before they reach the outer boundary, therefore yielding a nonreflective inflow boundary. The basic equation can be written in the following form[16,17]:

$$\frac{\partial \boldsymbol{q}}{\partial t} + R_d^{-1}(x)(\boldsymbol{q} - \boldsymbol{q}_0) = k(\boldsymbol{q}) \tag{6}$$

Here $k(\boldsymbol{q})$ denotes the flux of the system of differential equations (4) and (5).

At the inflow boundary region, which includes three grid lines in the outer boundary region, $\boldsymbol{q}_0 = \boldsymbol{0}$ is prescribed and the control coefficient of Newtonian friction $R_d^{-1}(x)$ reaches the maximum value at the terminal plane x_B and gradually decreases to zero toward the interior with a Gaussian half-width of b_{nt} as described by

$$R_d^{-1}(x) = R_d^{-1}(x_B)\exp\left\{-\ell n(2.0)[(x - x_B)/b_{nt}]^2\right\} \tag{7}$$

Sound Source BC

The sound source boundary is assumed to be located ahead of an aeroengine fan. Generally the inlet internal sound source BCs should serve two different purposes. On one hand they should excite the incoming duct acoustic modes propagating upstream toward the inlet plane. On the other hand, they must allow the reflected waves from an open end, a turning plane, or duct shape variation to leave the computational domain without reflection. To serve this role, a transition zone with 10 grid spacings from the source to the interior domain is introduced to force the numerical solutions to the analytical sound sources from the interior to the source boundary.

Following the idea of the Newtonian friction technique as expressed by Eq. (6), here $\boldsymbol{q}_0$ is set to the analytical sound source. In this way, reflected waves from the interior domain are absorbed gradually to the value of the sound source when they reach the sound source boundary. Additionally, short-wavelength oscillations arising from the abrupt change between the given sound source and the interior domain are reduced by the Newtonian buffer zone. Note that in a real aeroengine the waves reflected downstream could also interact with the fan or the exhaust, generating upstream-propagating sound waves, a process that is neglected in this formulation. Each upstream-propagating acoustic azimuthal mode excited at the source plane can be specified by the analytical solution for a radially constant mean flow as a set of radial modes of the given azimuthal mode for a circular or annular cylindrical duct:

$$\boldsymbol{q}_0 = \begin{pmatrix} \varrho' \\ u' \\ v' \\ w' \\ p' \end{pmatrix}_{mn} = A_{mn} \begin{pmatrix} NJ_m(\mu_{mn}r) + MY_m(\mu_{mn}r) \\ \dfrac{k}{\omega - M_x k}\left[NJ_m(\mu_{mn}r) + MY_m(\mu_{mn}r)\right] \\ -\dfrac{i\mu_{mn}}{\omega - M_x k}[NJ'_m(\mu_{mn}r) + MY'_m(\mu_{mn}r)] \\ \dfrac{m}{r(\omega - M_x k)}[NJ_m(\mu_{mn}r) + MY_m(\mu_{mn}r)] \\ \gamma\dfrac{\bar{p}}{\bar{\varrho}}[NJ_m(\mu_{mn}r) + MY_m(\mu_{mn}r)] \end{pmatrix} e^{i(\omega t - m\varphi - kx)} \tag{8}$$

where A_{mn} is the specified complex amplitude of the sound source and J_m and Y_m denote, respectively, the mth-order Bessel function of the first kind and the Neumann function. For the hard-wall cases, $v' = 0$, $M/N = -J'_m(\mu_{mn}R_1)/Y'_m(\mu_{mn}R_1)$. The usually complex

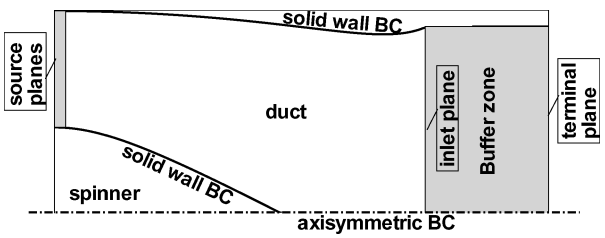

Fig. 1 BCs for a generic aeroengine inlet geometry.

wave number k in the axial direction is expressed in terms of the mean flow Mach number M_x (for the inlet cases, $M_x < 0$) for the upstream-propagating acoustic wave as

$$k = \frac{-\omega M_x + \sqrt{\omega^2 - \left(1 - M_x^2\right)\mu_{mn}^2}}{1 - M_x^2} \tag{9}$$

The cutoff ratio is defined as

$$\xi = \omega \Big/ \left(\mu_{mn}\sqrt{1 - M_x^2}\right) \tag{10}$$

An acoustic mode is cuton if $\xi > 1$. The mode is cutoff if $\xi < 1$ because the axial wave number k has a nonzero imaginary part.

To be consistent with the radial eigenvalue μ_{mn}, the excited sound source is assumed to be subjected to a uniform mean flow. However, the CFD calculated mean flow velocity of the two-dimensional Euler solution at the source plane $x = 0$ varies along the radial direction. This is different from the uniform mean flow at the source region employed in the FEM and MS computations.[10] The sound source BC should therefore be generalized such that it becomes suitable for radially varying mean flows, in the future thereby avoiding the errors and restrictions arising from the uniform mean flow assumption.

Solid-Wall BC

For the inviscid flow cases, the zero normal contravariant velocity condition should be satisfied at the curvilinear solid walls. Because a high-order DRP scheme is employed to discretize the governing equations, the number of BC required for a unique solution is large. Here the solid-wall BC proposed by Tam and Dong[18] with ghost values p' inside the wall is chosen for satisfying $\boldsymbol{V} \cdot \boldsymbol{n} = 0$, where $\boldsymbol{V}$ and $\boldsymbol{n}$ represent the contravariant velocity and normal vector, respectively.

Axial Boundary

For the three-dimensional axisymmetric approach, a special BC is needed on the axis. The BC is symmetric or antisymmetric depending on the azimuthal mode number m. Unlike the solid wall, three ghost lines below the symmetry line are used for the seven-point DRP scheme, which are calculated by the dependency on m. Inserting $\varphi = \pi$ for a point below the symmetry line, one obtains the coefficient $\Re\mathfrak{e}\{e^{-im\pi}\} = (-1)^m$ for the mirrored points below the axis.

For the velocity components, the axial BC has to be formulated in the index-coordinate system that is used above the axis, as the cylindrical coordinate system uses a basis of vectors rotated 180 deg around the x axis. Observing the fact that, unlike the cylindrical coordinates, the index coordinates i and j maintain their direction for the mirrored points, the sign of the v' and w' velocity components must be changed again. The axial boundary conditions can thus be expressed as

$$p'(-r) = (-1)^m p'(r) \tag{11}$$

$$\varrho'(-r) = (-1)^m \varrho'(r) \tag{12}$$

$$u'(-r) = (-1)^m u'(r) \tag{13}$$

$$v'(-r) = -(-1)^m v'(r) \tag{14}$$

$$w'(-r) = -(-1)^m w'(r) \tag{15}$$

Another problem is the singularity of the cylindrical coordinates at the axis (for $r \to 0$). The terms of $(1/r)\bar{\varrho}(v'_m - imw'_m)$ and $(1/r)\varrho'_m \bar{V}$ and the terms of $(1/r)\bar{V}w'_m$ and $(1/\bar{\varrho})(im/r)p'_m$ in Eq. (4) must be considered in order to avoid singularities. Here the product $(1/r)C \cdot q$ involved in these singularity terms is replaced by its limit value as

$$\lim_{r \to 0} \frac{1}{r} C \cdot \boldsymbol{q} = C \cdot \frac{\partial \boldsymbol{q}}{\partial r} \tag{16}$$

From physical considerations, it is clear that none of the ratios can approach infinity; hence, this singularity must be discussed for each azimuthal mode with respect to its particular physics. The axisymmetric mean flow has no component orthogonal to the axis at the singularity. The radial flow velocity component $\bar{V}$, tends to zero faster than r, and therefore the terms $(1/r)\bar{V}\varrho'_m$ and $(1/r)\bar{V}w'_m$ are zero at the axis. The C in Eq. (4) can then be simplified to

$$C = \begin{pmatrix} 0 & 0 & \bar{\varrho} & m\bar{\varrho} & 0 \\ 0 & 0 & 0 & 0 & 0 \\ 0 & 0 & 0 & 0 & 0 \\ 0 & 0 & 0 & 0 & -\dfrac{m}{\bar{\varrho}} \end{pmatrix} \tag{17}$$

The two terms that remain to be considered in C, are now discussed for different azimuthal modes. For $m = 0$, only the v'_m/r term has to be replaced by its limit value, $\partial v'_m/\partial r$. Thus C in Eq. (17) is reduced and replaced by C_0 as expressed in Eq. (18). For $m = 1$, the term $v'_m - iw'_m$ equal to zero, p'_m/r is replaced by its limit value, $\partial p'_m/\partial r$, and C is replaced by C_1 as shown in Eq. (18). For $m = 2$, only $(v'_m - imw'_m)/r$ is replaced by its limit value, $\partial(v'_m - imw'_m)/\partial r$, and C is replaced by C_2 as seen in Eq. (18):

$$C_0 = \begin{pmatrix} 0 & 0 & \bar{\varrho} & 0 & 0 \\ 0 & 0 & 0 & 0 & 0 \\ 0 & 0 & 0 & 0 & 0 \\ 0 & 0 & 0 & 0 & 0 \end{pmatrix}, \qquad C_1 = \begin{pmatrix} 0 & 0 & 0 & 0 & 0 \\ 0 & 0 & 0 & 0 & 0 \\ 0 & 0 & 0 & 0 & 0 \\ 0 & 0 & 0 & 0 & -\dfrac{m}{\bar{\varrho}} \end{pmatrix}$$

$$C_2 = \begin{pmatrix} 0 & 0 & \bar{\varrho} & m\bar{\varrho} & 0 \\ 0 & 0 & 0 & 0 & 0 \\ 0 & 0 & 0 & 0 & 0 \\ 0 & 0 & 0 & 0 & 0 \end{pmatrix} \tag{18}$$

At the axis, higher modes ($m > 2$) behave like the mth-order Bessel function of the first kind. Then C in Eq. (17) can be completely neglected because the φ derivatives at the axis reach faster to zero than r:

$$C_m \equiv \boldsymbol{0}, \qquad m > 2 \tag{19}$$

Results and Discussion

Validation Using Hard-Walled Circular and Annular Ducts

The CAA procedure is first validated by a straight circular and a straight annular hard-walled infinite duct with upstream propagation of acoustic modes through subsonic uniform mean flows. The necessary appropriate BCs for both the circular and annular ducts are merely simplifications from the arrangement for a complicated aeroengine inlet duct geometry as sketched in Fig. 1. In both cases, the sound sources are excited against the uniform mean flow of $M_0 = -0.5$. Because the cross section and mean flow are constant for both validation cases, there are no reflection waves from the inflow regions. Hence the numerical results can be compared with analytical upstream wave solutions.

In the circular duct case, a uniform grid with $\Delta x = \Delta r = 1/32$ is distributed in the interior domain along both the $x-$ and $r-$ directions. The total number of grid points used in the computation is 120×37 including a stretched buffer zone. The grid resolution is 13 PPW along the x direction in the interior domain. Figure 2 gives the instantaneous wall pressure comparison between numerical and analytical solutions for $m = 6$, $n = 1$, $\omega = 10$, with the buffer zone not shown. There is a good agreement of the numerical and the analytical results.

For the annular duct case, the outer wall radius is $R_2 = 1$ and the inner wall radius is $R_1 = 0.42356$. Uniform grids are distributed along both the x and r directions in the interior domain. The grid is stretched in the x direction to obtain a longer buffer zone at low computational costs. The total number of grid points is 120×35.

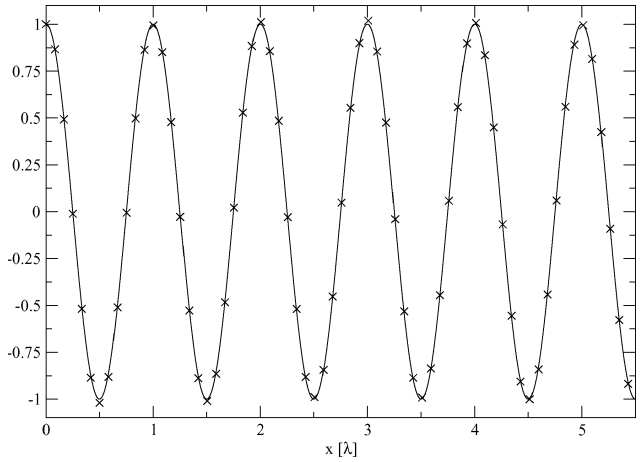

Fig. 2 Normalized instantaneous wall pressures along a cylindrical circular duct ($m=6$, $n=1$, $\omega=10$, $M_0=-0.5$): ×, CAA and ——, analytical.

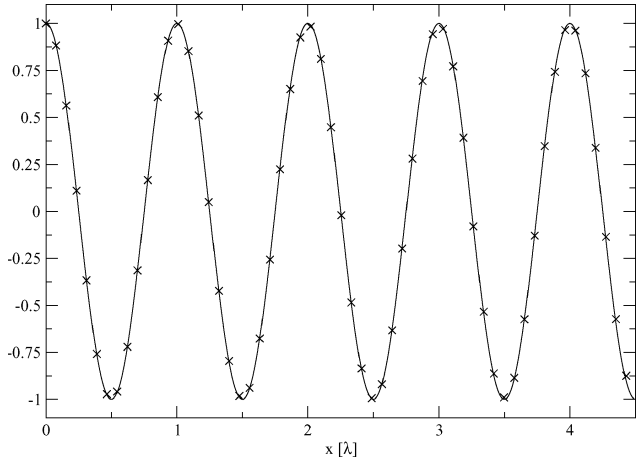

Fig. 3 Normalized instantaneous outer wall pressures along a cylindrical annular duct ($m=10$, $n=1$, $\omega=16$, $M_0=-0.5$): ×, CAA and ——, analytical.

The grid resolution is about 14 PPW along the x direction in the interior domain. The instantaneous outer wall pressure comparison between CAA and analytical solutions at $m=10$, $n=1$, $\omega=16$ is shown in Fig. 3, with the buffer zone not shown. The numerical results agree well with the analytical solutions.

The two basic validation cases have proved the accuracy of the numerical schemes as well as the various BCs. In particular, it is noteworthy that the buffer zone BC is very reliable and robust in the inflow region. It has also worked well in conjunction with the prescribed sound source, rendering a nonreflective sound source BC for computations.

Comparison Between the CAA, FEM, and MS Solutions for Accoustic Duct Mode Propagation in an Axisymmetric Aeroengine Inlet Duct

An axisymmetric inlet with aeroenginelike geometry from the paper of Rienstra and Eversman[10] is selected for further benchmarking, as a range of semi-analytic and purely numerical test cases are available for comparison. The outer and inner wall radii of the inlet geometry, R_2 and R_1, are described by

$$R_2(x) = 1 - 0.18453x'^2 + 0.10158\frac{e^{-11(1-x')} - e^{-11}}{1-e^{-11}} \quad (20)$$

$$R_1(x) = \max\left[0,\, 0.64212 - (0.04777 + 0.98234x'^2)^{\frac{1}{2}}\right] \quad (21)$$

where $x' = x/L$, $L = 1.86393$, $R_1(0) = 0.42356$, and the spinner tip is located at $x = 1.13547$.

Equations (20) and (21) define the duct shape from the source plane $x=0$ to the inlet plane $x=1.86393$. The duct is extended from the inlet plane $x=1.86393$ to the terminal plane $x=3.0$ to allow the flowfield to become uniform at the terminal plane. For CAA computations, the extended domain will serve as a Newtonian friction-based buffer zone to absorb inflow disturbances. A sketch of the duct inlet together with the prescribed BCs for the CAA simulation is shown in Fig. 1. Body-fitted grids are generated for all of the CAA computations with 451×151 points in the x and r directions, respectively. The employed DRP scheme has a spatial resolution of approximately seven PPW. For the highest frequency case (calculated in this paper) of $\omega=50$, $M_0=-0.5$, $m=40$, $n=1$, there are about 18 PPW in the axial direction. The number of grid points provides a resolution of at least 12 PPW for the modes and frequencies shown in this paper. To check the accuracy, a refined mesh (in both directions) with 901×301 points has been generated to calculate the case of highest frequency and azimuthal mode number. To reduce the computation time, the grids have been split into evenly distributed multiblocks for parallel computations.

Mean Flowfield

The mean flow is assumed to be two-dimensional in the axisymmetric geometry, such that there is no swirling component ($\bar{W}=0$). A low-order CFD Euler solution was used to compute the mean flowfield as a basis for the sound propagation simulation. The calculated mean flowfield is shown in Fig. 4, where $M_0 = -0.5$ is an averaged mean flow Mach number at the source plane $x=0$. The entropy distribution generated by CFD is not exactly constant due to numerical errors especially around the spinner tip and duct lip regions. However, these nonhomentropic regions are very limited and the disturbance in the speed of sound $a^2 = \gamma(\bar{p}/\bar{\varrho})$ is first order with respect to the perturbation quantities. The products of the perturbation quantities and the disturbance of homentropy are therefore second order. The entire mean flowfield can be approximated as homentropic, which is consistent with the acoustic computations.

Because of the differing requirements for CFD and CAA calculations, both procedures need different grids. This requires an interpolation of the mean flowfield from the CFD grid to the CAA grid. A routine for this interpolation has been provided by DLR.[19] Figure 4 shows that the mean flowfield varies in both the radial and axial directions, even at the source plane $x=0$.

There are differences in the mean flow solution among the CAA, FEM, and MS methods. The FEM computations are based on a two-dimensional potential mean flow, which is very close to that used in the CAA computations. The CAA mean flow is nonuniform throughout the duct; however, the FEM and MS mean flow velocities are uniform at the source plane $x=0$. Unlike the CAA and FEM methods, the mean flow in MS is based on a quasi-one-dimensional solution. It is expected that these differences should result in deviations in the acoustic computation results.

Furthermore the sound source also requires a uniform mean flow in the CAA computations. This difference causes the inconsistency at the source boundary region in the CAA computations. For this reason, it should be expected that higher radial modes will be observed in the current CAA numerical results. It is, however, anticipated that an alleviation will occur through either the introduction of a straight annular duct transition zone between the sound source plane and the section of variable area or the reformulation of the sound source for variable flow occurrences.

Acoustic Field

A large number of numerical tests have been carried out with parameter variations of m, n, ω, and M_0. In the interest of brevity, only two typical cases are presented.

First, the numerical results for the $m=10, n=1, \omega=16$ case with mean flow at $M_0=-0.5$ is presented in Fig. 5 and compared with the solutions of the FEM and MS methods.[10] The main pattern of the CAA results agree well with the FEM and MS solutions. However, the CAA solutions are much closer to the FEM solutions. There are two main reasons for this: First, both the CAA and FEM numerical methods permit the propagation of many modes and scattering is

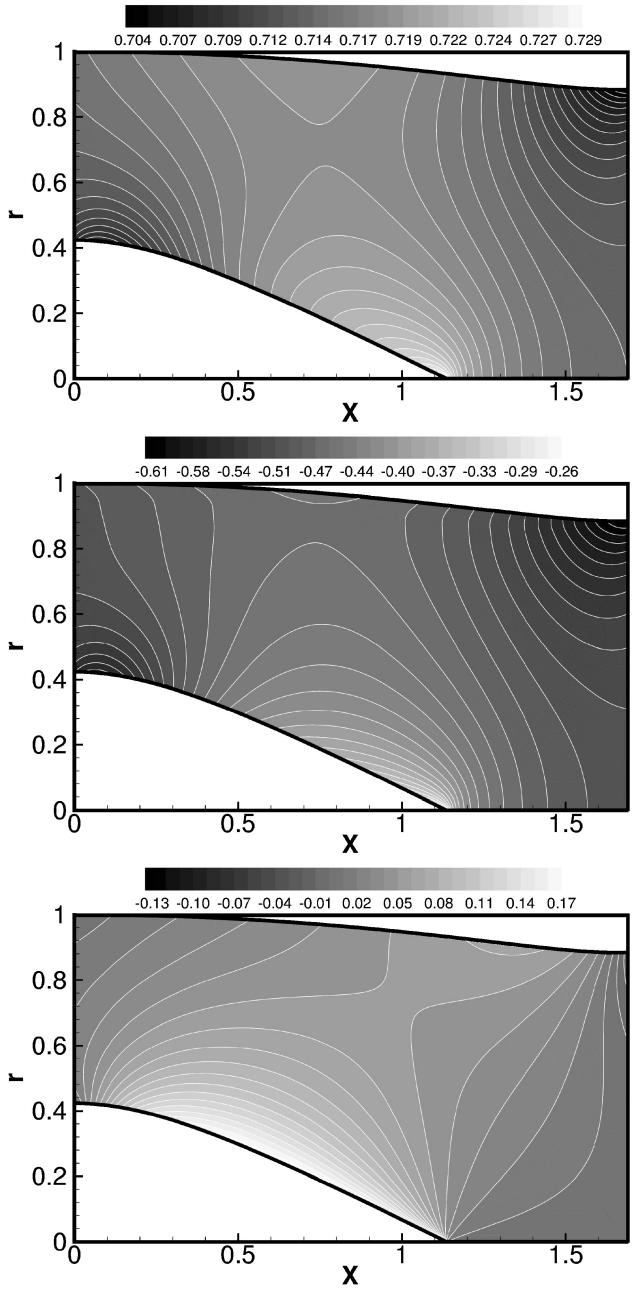

Fig. 4 Normalized mean flow contours, CFD Euler solution, $M_0 = -0.5$. Top down: normalized pressure and the velocity components $\bar{U}$ and $\bar{V}$.

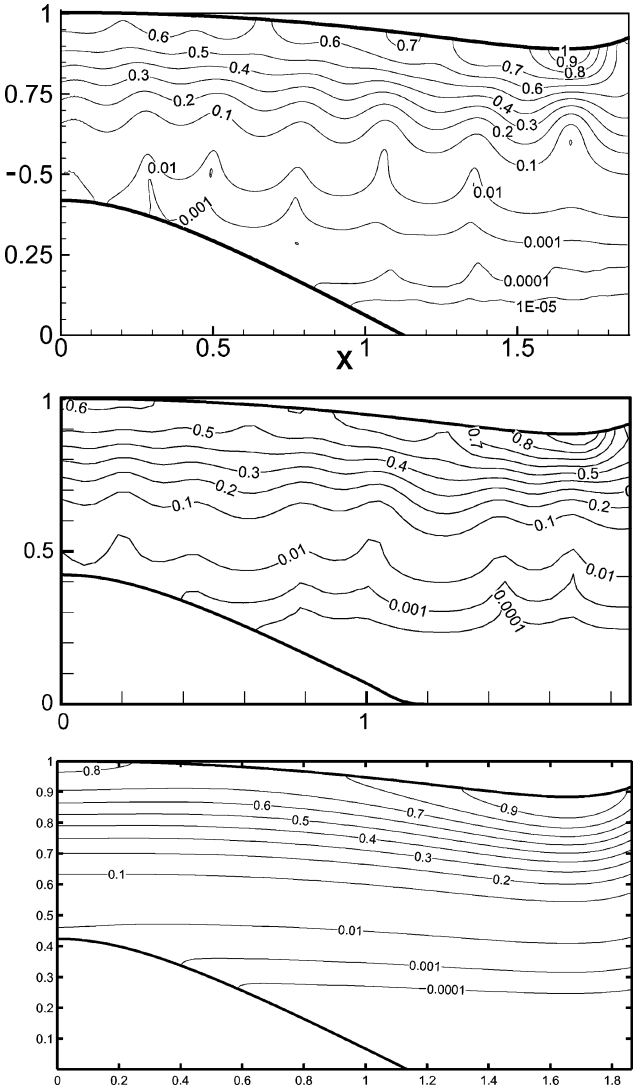

Fig. 5 Normalized pressure contours ($M_0 = -0.5$, $m = 10$, $n = 1$, $\omega = 16$). Top down: CAA, FEM, and MS.

incorporated in the numerical solutions, whereas the MS method assumes that a single mode does not scatter into other modes in the gradually varying duct. Based on Eq. (10), the cutoff ratio ξ is approximately 1.57 at $x = 0$ for the case of $m = 10$, $n = 1$, $\omega = 16$, and $M_0 = -0.5$. Theoretically, the second radial mode ($m = 10$, $n = 2$, $\omega = 16$, $M_0 = -0.5$) is also cuton with $\xi \approx 1.124$ at $x = 0$. This implies that the second radial mode is capable of being scattered and of interfering with the excited first radial mode in both the CAA and FEM solutions. However, no interference between modes should occur in the MS solution due to the WKB assumption of each mode in the slowly varying duct. The second reason is that both the CAA and FEM solutions include the reflected modal amplitudes from the duct and mean flow variations, particularly from the duct lip and inlet plane regions. But the left- and right-running waves have been explicitly given in the MS solution, which has excluded the reflection characteristics apparent in the real physics. Therefore the CAA and FEM solutions have clear interference patterns and some visible wiggles, whereas the MS exhibits very smooth contours. Higher radial modes can be observed for both FEM and CAA especially around $x = 0.2$, 1.0, and 1.6, where a higher pressure amplitude at the casing appears together with a minimum value at around $x = 0.5$.

Comparing carefully the CAA and FEM solutions, some differences can be observed near the hard-wall boundary region, particularly in the lip and spinner tip regions. This deviation is mainly attributed to the different mean flows used in the respective calculations. Compared with mean flow used in the FEM calculations,[10] the mean flows used in the CAA calculations have stronger radial and axial variations (as seen in Fig. 4). It would be possible to use an equivalent mean flow for exact comparison; however it is not absolutely required because the observed difference between the CAA and FEM methods is already very minimal.

Variations in frequency ω and the azimuthal mode number m can lead to different propagation patterns. Given a fixed azimuthal mode number m and radial mode number n, the cutoff ratio ξ at the source plane $x = 0$ will increase with increasing frequency. To give an example, ξ will be increased to about 4.905 if ω is set to 50 for the case of $m = 10$, $n = 1$, $M_0 = -0.5$. Then 11 radial modes will be cuton and the first radial mode will interfere with 10 scattered higher radial modes. Several CAA solutions have been compared with the FEM and MS solutions with a good agreement and will not be presented here.

With respect to an increase in azimuthal mode number m, the radial wave number of the primary first radial mode will be increased. Figure 6 shows a comparison of results for $m = 40$, $n = 1$, $\omega = 50$,

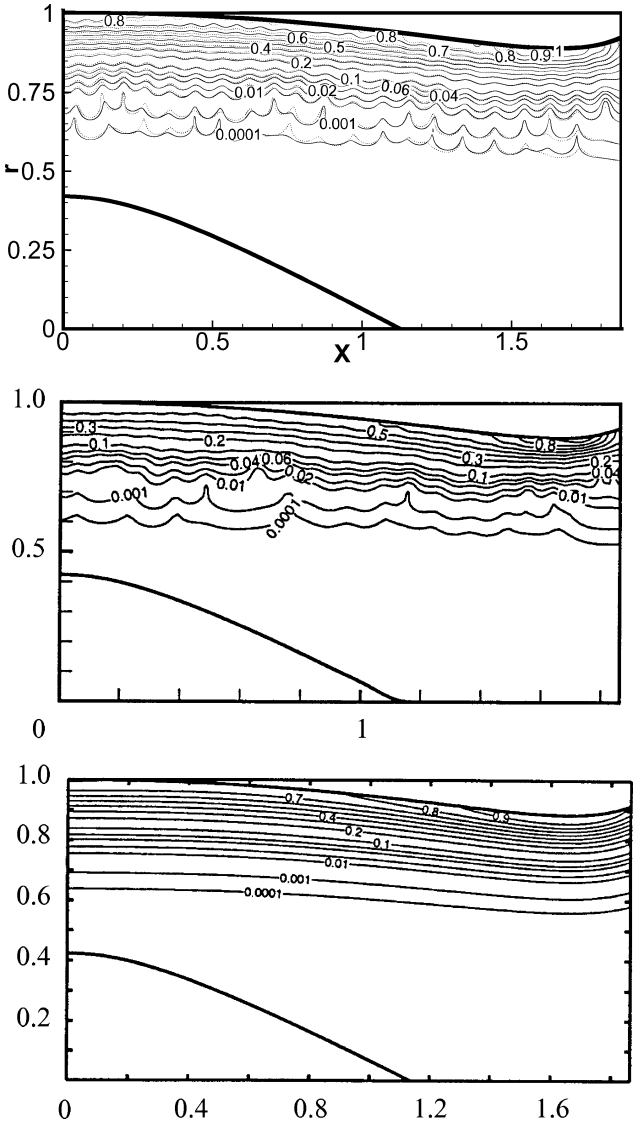

Fig. 6 Normalized pressure contours ($M_0 = -0.5$, $m = 40$, $n = 1$, $\omega = 50$). Top down: CAA, FEM, and MS. In the CAA results, the solid and dotted lines were calculated based on the coarse and refined grids, respectively.

and $M_0 = -0.5$. In this case, the cutoff ratio ξ at $x = 0$ is about 1.35 for the first radial mode. Theoretically the first three radial modes are cuton. In Fig. 6, the CAA results were calculated based on both the coarse mesh (solid lines, with 451×151 grid points) and the refined mesh (dotted lines, with 901×301 grid points). Both contour lines agree well; only very small differences can be observed at the very low amplitude regions. The numerical solutions (CAA, FEM) for $m = 40$ agree better with the MS solutions compared with the agreement at the lower azimuthal mode case of $m = 10$. However, wiggles in the CAA and FEM solutions are still visible because of scattering of higher radial modes.

In general, the CAA solutions agree well with the FEM and MS solutions. This indicates that the proposed CAA procedure has comparable properties for predicting the sound propagation in ducts with complex geometry and flow physics, while employing a different numerical method with assumptions different from those of FEM and MS in the solution.

Numerical Study of the Hard-Walled Cuton and Cutoff Transition Phenomena in an Axisymmetric Aeroengine Inlet Duct

To show the capability of the proposed CAA procedure, the hard-walled cuton and cutoff transition phenomenon is investigated for the same axisymmetric aeroengine inlet duct with geometry defined by Eqs. (20) and (21).

The cuton and cutoff transition of a mode in a hard-wall flow duct is also known as a turning point problem. It was studied by Nayfeh and Telionis[20] for the no-flow case and was recently extended to include flow effects by Rienstra.[21] In the case of no flow, the transition or turning points are solely determined by the variation of duct geometry that is mathematically described by the cutoff ratio ξ. The portions of the duct for which $\omega > \mu_{mn}$ are defined as cuton regions, whereas those for which $\omega < \mu_{mn}$, where the imaginary part of the axial wave number is nonzero, are known as cutoff regions. The axial positions at which $\omega = \mu_{mn}$ are called the transition or turning points. A direct practical application is to reduce the acoustic energy in a duct by gradually decreasing and then increasing its cross-sectional area,[20] as the imaginary part of the wave number is connected to a decaying amplitude of the related mode. Rienstra's study[21] further showed that the usual turning point behavior could also be found in a slowly varying hard-walled duct with irrotational isentropic mean flow. In addition to the geometric effect, the mean flow effect must be included for cases incorporating a mean flow. Theoretically the turning plane is located at the position where $\omega = \mu_{mn}\sqrt{(1 - M_x^2)}$.

The decaying mode can propagate only for cases with mean flow. In the no-flow case, the axial wave number is zero at the turning plane, which is related to an infinite axial wavelength c, and the acoustic wave will not propagate forward with a wavefront normal to the duct wall. Because of the conservation of the acoustic energy in case of homentropic mean flow, the turning plane must excite a reflected wave transferring the energy backward to the sound source region. With mean flow, there is a transmitted cutoff wave with wave number $k = -\omega M_x$. The reflected and incoming waves both have positive wave numbers related to phase velocities opposed to the flow direction. Nonetheless, the group velocity associated with energy transport is positive only for the incoming wave. Therefore a pattern of positive and negative interference between the incoming and reflected waves should be observed for each turning point. The sound source has to be nonreflective to the reflected wave in this case.

Here the nonconvective hard-walled cuton and cutoff transition case is first studied by the proposed CAA approach. Figure 7 gives the isopressure distribution with $m = 10$, $n = 1$, $\omega = 12$, and $M_x = 0$. For checking the CAA results, the cutoff line ($\xi = 1$) is also depicted in Fig. 7 based on the analytical eigenvalue solutions for μ_{mn}, assuming an annular cylindrical duct. Theoretically the excited sound mode is only slightly cuton with $\xi \approx 1.0195$ at $x = 0$ and becomes cutoff at $x \approx 0.19$. This means that $x \approx 0.19$ is the theoretically predicted turning plane. The numerical calculation results from CAA show that the sound wave at $x < 0.23$ is fully cuton, whereas it decays very quickly for $x > 0.23$. Thus the calculated turning plane from CAA is located around $x = 0.23$ with a good agreement with the theoretically predicted position.

Furthermore, a cuton and cutoff transition case is shown in Fig. 8 based on an Euler mean flow (as shown in Fig. 4 with $M_0 = -0.5$) for $m = 10$, $n = 1$, $\omega = 11.129$. The variation of the flow is rather strong especially around the spinner and the lip region, which violates the

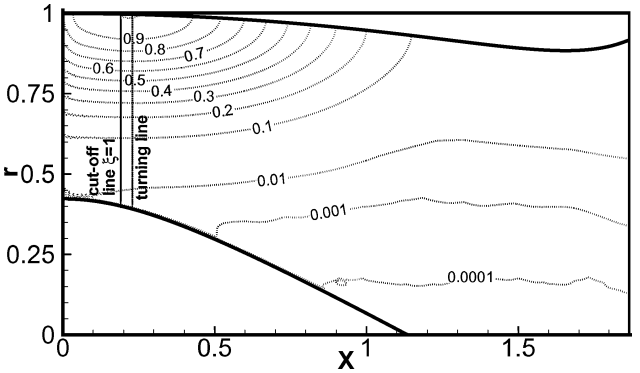

Fig. 7 Normalized pressure contours for the cuton and cutoff transition case ($M_0 = 0$, $m = 10$, $n = 1$, $\omega = 12$). The turning plane is situated around $x = 0.23$.

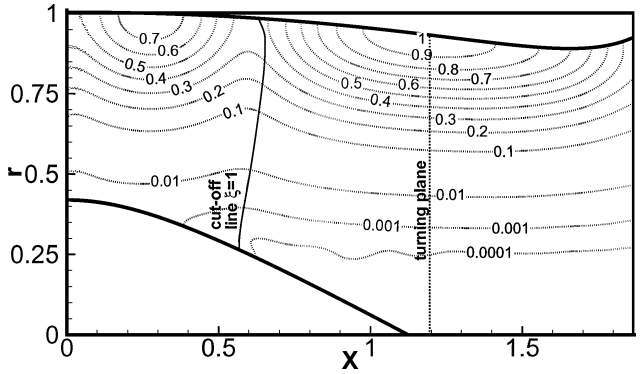

Fig. 8 Normalized pressure contours calculated based on an Euler mean flow (see Fig. 4) ($m = 10$, $n = 1$, $\omega = 11.129$, $M_0 = -0.5$). The CAA predicted turning plane is situated around $x = 1.2$.

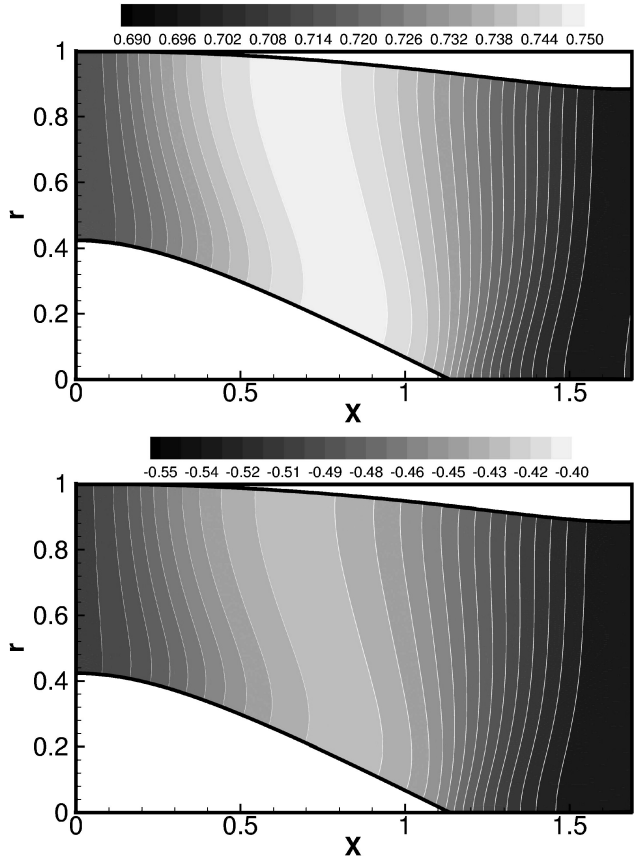

Fig. 9 Normalized pressure $\bar{p}$ contours (top) and axial velocity component $\bar{U}$ (bottom) of the quasi-one-dimensional potential mean flow used in Fig. 10.

assumption of uniform mean flow. The approximated turning plane based on Eq. (9) is located at $x \approx 0.6$. However, the CAA calculated results show a standing wave pattern at $x < 1.2$ and a decaying wave pattern from $x > 1.2$. This is done in spite of the rough approximation of the real flow conditions due to the variable geometry. This means that the CAA calculated turning plane is roughly located at $x = 1.2$, whereas the analytical solution locates it at $x \approx 0.6$, in a radially relatively constant mean flow. The conclusion is therefore that the shown radial variation of the flow in a real engine inlet has a vital influence on the turning behavior.

This sizable deviation is suspected to be due to the spatial variation of the mean flowfield. For testing this hypothesis, a slightly spatially varying quasi-one-dimensional potential mean flow is calculated with $M_0 = -0.5$ for the same duct geometry as shown in Fig. 9;

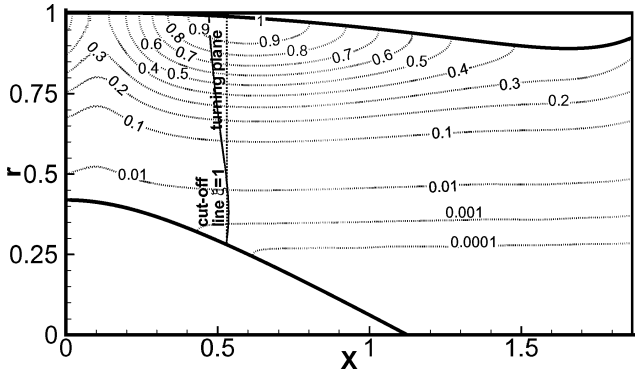

Fig. 10 Normalized pressure contours calculated based on quasi-one-dimensional potential mean flow (see Fig. 9) of $M_0 = -0.5$ at $m = 10$, $n = 1$, $\omega = 11.129$. The CAA predicted turning plane is situated around $x = 0.52$.

the pressure in the flow is kept constant along grid lines. The CAA results as well as the theoretical cutoff ratios for the same duct mode are calculated again as shown in Fig. 10. It is very interesting to find that the CAA-predicted turning plane lies very close to the theoretically predicted position $x \approx 0.52$. It can be observed that the turning plane based on this artificial potential mean flow is much closer to the sound source region than that of the real Euler mean flow. Additional numerical results for a very high azimuthal mode transition case has found a similar phenomenon. Therefore it can be concluded that the cuton and cutoff behavior not only is dependent on the duct geometry but is also very sensitive to the basic mean flowfield.

Considering the available theoretical studies for the no-flow case by Nayfeh and Telionis[20] and for the irrotational isentropic mean flow case using the slowly variable duct approximations by Rienstra,[21] the investigation in this paper provides an additional understanding about the cuton and cutoff transition behavior in complex mean flow ducts. In particular, the physical correctness of the mean flow is crucial for the accurate prediction of the turning plane.

Conclusions

A three-dimensional axisymmetric CFD/CAA approach is proposed to simulate sound wave propagation in axisymmetric duct flows. The main idea is to calculate each azimuthal mode using a Fourier transform and decomposition for the azimuthal coordinate φ. Optimized high-order schemes are employed for both the space discretization and time stepping. A buffer-zone-type BC has been found to be very reliable and stable, while offering the possibility to formulate an accurate nonreflective sound source boundary condition. The proposed procedure has been validated successfully using a number of different examples.

Furthermore, the acoustic mode cuton/cutoff transition phenomenon in a hard-walled duct is studied for no-flow as well as flow cases. Two different mean flow assumptions have been compared with special attention to the turning plane. The turning plane predicted with an artificial quasi-one-dimensional potential flow agrees well with the theoretically predicted location. However, the numerical results based on the real two-dimensional Euler flow deviate from the analytical results. This indicates that the mean flow plays a very important role in the determination of the turning plane in addition to the known duct geometry effect.

The main advantages of the proposed three-dimensional axisymmetric CFD/CAA approach are twofold. First, it is very efficient compared with full three-dimensional computations for axisymmetric duct flows. Second, this approach is rather straightforward and its suitability can be extended to more complex mean flow cases, such as nonhomentropic mean flows (through the introduction of the energy equation) or flows with swirl, which forms the focus of current work. The soft-wall BC has not been implemented in the present procedure, but its development and validation is planned in the near future. One drawback of the three-dimensional axisymmetric approach is

that it cannot be applied to a fully three-dimensional flow and geometry, such as a scarfed inlet. Therefore, fully three-dimensional numerical methods are still necessary in certain cases.

Acknowledgments

This work was carried out in the framework of the European Community project TurboNoiseCFD and the DFG SWING+ project. The first author (X. D. Li) was partially supported by NSFC-50076002 and ASFC-01C51036. The authors thank S. W. Rienstra and W. Eversman for their kind permission to use their MS and FEM solutions for comparison. The authors are grateful to the referees for carefully reviewing the manuscript and providing valuable comments.

References

[1]Ozyoruk, Y., and Long, L. N., "Computation of Sound Radiating from Engine Inlets," *AIAA Journal*, Vol. 34, No. 5, 1996, pp. 894–901.

[2]Ait-Ali-Yahia, D., Stanescu, D., Robichaud, M. P., and Habashi, W. G., "Spectral Element Grid Generation and Nonlinear Computations for Noise Radiation from Aircraft Engines," AIAA Paper 99-1832, May 1999.

[3]Ahuja, V., Ozyoruk, Y., and Long, L., "Computational Simulation of Fore and Aft Radiation from Ducted Fans," AIAA Paper 2000-1943, June 2000.

[4]Druault, P., Gerolymos, G. A., and Nousis, I., "Comparison of Theoretical and Computational Results of Spinning Acoustic Modes Propagation in Aircraft Engine Intakes," 5th CEAS–ASC Workshop on "Turbomachinery Noise and Duct Acoustics," Eindhoven Univ. of Technology, Eindhoven, The Netherlands, Nov. 2001.

[5]Eversman, W., Parret, A. V., Preisser, J. S., and Silcox, R. J., "Contributions to the Finite Element Solution of the Fan Noise Radiation Problem," *Journal of Vibration, Acoustic, Stress and Reliability in Design*, Vol. 107, April 1985, pp. 215–223.

[6]Rienstra, S. W., "Sound Transmission in Slowly Varying Circular and Annular Ducts with Flow," *Journal of Fluid Mechanics*, Vol. 380, Feb. 1999, pp. 279–296.

[7]Dunn, M. H., Tweed, J., and Farassat, F., "The Prediction of Ducted Fan Engine Noise via a Boundary Integral Equation Method," AIAA Paper 96-1770, May 1996.

[8]Eversman, W., "Mapped Infinite Wave Envelope Elements for Acoustic Radiation in a Uniformly Moving Medium," *Journal of Sound and Vibration*, Vol. 224, No. 4, 1999, pp. 665–687.

[9]Astley, R., Hamilton, J., Baker, N., and Kitchen, E., "Modelling Tone Propagation from Turbofan Inlets—The Effect of Extended Lip Liners," AIAA Paper 2002-2449, June 2002.

[10]Rienstra, S. W., and Eversman, W., "A Numerical Comparison Between the Multiple-Scale and Finite-Element Solution for Sound Propagation in Lined Flow Ducts," *Journal of Fluid Mechanics*, Vol. 437, June 2001, pp. 367–384.

[11]Tam, C. K. W., and Webb, C., "Dispersion-Relation-Preserving Finite Difference Schemes for Computational Aeroacoustics," *Journal of Computational Physics*, Vol. 107, No. 2, 1993, pp. 262–281.

[12]Tam, C. K. W., "Computational Aeroacoustics: Issues and Methods," *AIAA Journal*, Vol. 33, No. 10, 1995, pp. 1788–1796.

[13]Hu, F. Q., Hussani, M. Y., and Manthey, J. L., "Low-Dissipation and Low-Dispersion Runge–Kutta Schemes for Computational Acoustics," *Journal of Computational Physics*, Vol. 124, No. 1, 1996, pp. 177–191.

[14]Stanescu, D., and Habashi, W. G., "2N-Storage Low-Dissipation and Low-Dispersion Runge–Kutta Schemes for Computational Aeroacoustics," *Journal of Computational Physics*, Vol. 143, No. 2, 1998, pp. 674–681.

[15]Tam, C. K. W., Webb, C., and Dong, T. Z., "A Study of Short Wave Components in Computational Aeroacoustics," *Journal of Computational Acoustics*, Vol. 1, March 1993, pp. 1–30.

[16]Li, F., Tam, C. K. W., and Choudhari, M., "Numerical Boundary Conditions for Simulation of Gust-Cascade Interaction," AIAA Paper 99-1845, May 1999.

[17]Israeli, M., and Orszag, S. A., "Approximation of Radiation Boundary Condition," *Journal of Computational Physics*, Vol. 41, No. 1, 1981, pp. 115–135.

[18]Tam, C. K. W., and Dong, Z., "Wall Boundary Conditions for High-Order Finite Difference Schemes in Computional Aeroacoustics," *Theoretical and Computational Fluid Dynamics*, Vol. 6, Oct. 1994, pp. 303–322.

[19]Lummer, M., Groggers, H. A., and Delfs, J. W., "Using RANS Mean Flow Fields in Numerical Aeroacoustics Simulation (CAA)," NATO RTO–AVT Symposium on Ageing Mechanism and Control, Pt. A—Developments in Computational Aero-and Hydro-Acoustics, Manchester, England, U.K., Oct. 2001.

[20]Nayfeh, A. H., and Telionis, D., "Acoustic Propagation in Ducts with Varying Cross Sections," *Journal of the Acoustical Society of America*, Vol. 54, No. 6, 1973, pp. 1654–1661.

[21]Rienstra, S. W., "Sound Propagation in Slowly Varying Lined Flow Ducts of Arbitrary Cross Section," *Journal of Fluid Mechanics*, Vol. 495, Nov. 2003, pp. 157–173.

W. Devenport
Associate Editor